Cobalt nanoparticle catalysed graphitization and the effect of metal precursor decomposition temperature

Stuart J Goldie[1], Shan Jiang[1], Karl S Coleman[1]

1. *Department of Chemistry, Durham University, South Road, Durham, DH1 3LE, UK*

Corresponding Author: k.s.coleman@durham.ac.uk

Thermal Analysis

Thermal analysis data from the carbon foams after acid washing to remove metals are presented below. The combustion profile in air is discussed within the main article. The metal free and $CoCl_2$ samples both show very similar profiles although the $CoCl_2$ catalysed carbon shows a more stable phase at the bottom. The higher temperature of the $Co(OAc)_2$ is evidence of better graphitization whilst the lower burn temperature of the $Co(NO_3)_2$ is due to the residual nanoparticles catalysing the combustion at lower temperatures. Key onset and inflection points were calculated for the different materials as shown below, the carbon from the $CoCl_2$ precursor clearly shows two distinct drops in mass which are analysed separately as listed in Table S 1. The gentle change in gradient from the $CO(NO_3)_2$ sample cannot be separated into multiple combustion events in contrast, the derivative plot shows a steady increase in rate of combustion to the inflection point at 625 °C with no secondary peaks. This is attributed to the catalytic effect of nanoparticles reducing the activation energy sufficiently that combustion is observed to take place at lower temperatures than possible from the other carbon samples, although this low temperature combustion is slow initially as the temperature rises the rate of mass loss to combustion rapidly increases. Despite this, the temperature of maximum mass loss is remarkably close to the other carbon materials.

Table S 1: Temperatures for onset and peak combustion rate for the different carbon materials. The onset is calculated by interpolating straight lines along the TGA plot from the inflection point and starting mass; the inflection points are calculated from the derivative plots shown in Figure S 3.

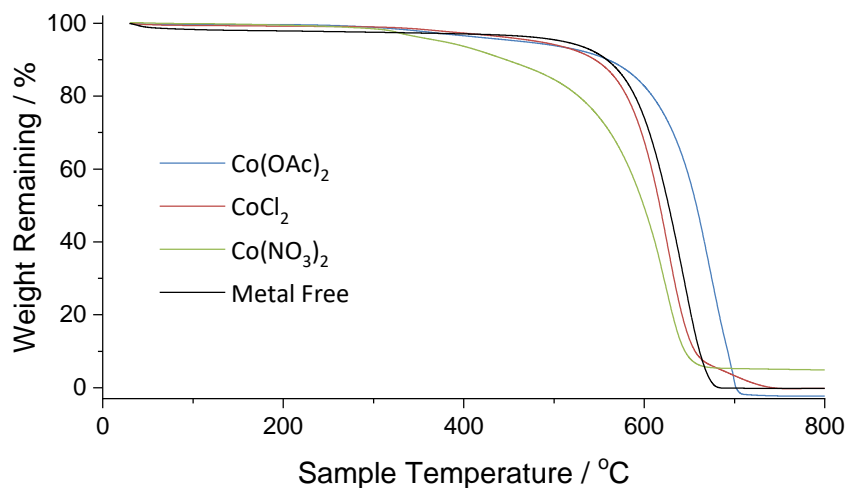| Sample	Onset / °C	Inflection Point / °C
$Co(OAc)_2$	625	675
$CoCl_2$ – amorphous domain	580	625
$CoCl_2$ – graphitic domain	650	700
$Co(NO_3)_2$	350	625
Metal Free Control	580	645

Figure S 1: TGA mass loss profiles in air of all carbon foams after acid washing, samples pressed into pellets and heated at 10 °C / min, constant gas flow of 30 mL/min.

Heating under an inert atmosphere liberates functional groups that are less strongly bound to the carbon material. The carbon foams prepared in this work show relatively small mass losses under such conditions. The control foam without catalyst has very little mass loss after the initial loss of water adsorbed to the surface and the high temperature mass loss is likely caused by trace oxygen present in the gas line. The graphitic foams produce by in-situ reduction of the metal salts have some mass loss above 400°C that indicates slight functionalization of the material but overall most of the mass remains.
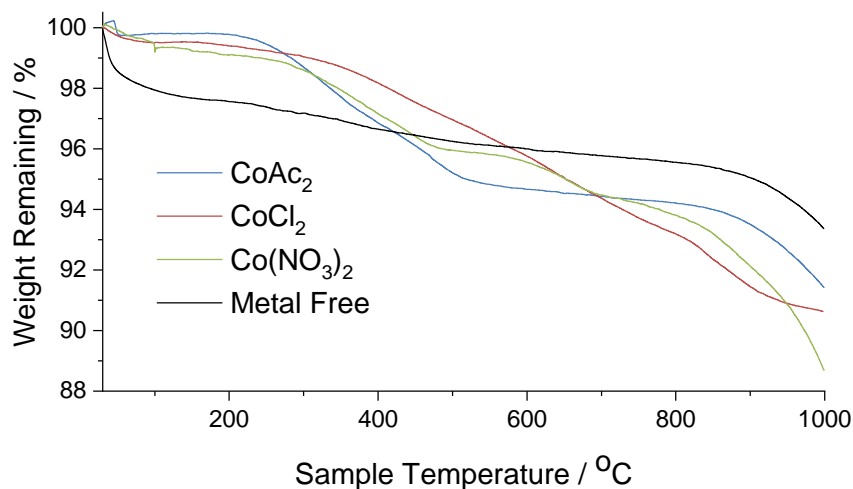
Figure S 2: TGA mass loss profiles in inert nitrogen of all carbon foams after acid washing, samples pressed into pellets and heated at 10 °C / min, constant gas flow of 30 mL/min.
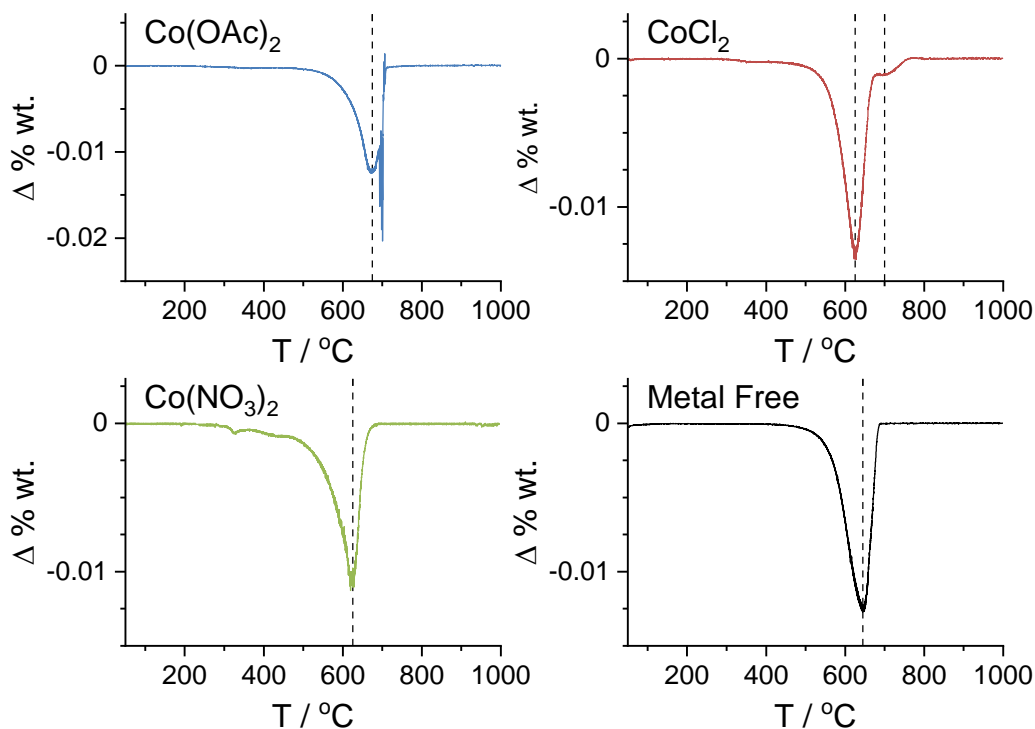
Figure S 3: First derivative plots of thermal gravimetric analysis from each material, labelled top left with the inflection points of maximum combustion marked with dashed lines. The $CoCl_2$ sample has both components marked.

Thermal analysis of the cobalt salts under a reducing atmosphere of 5% H_2 in Ar was completed and the waste gas stream analysed by mass spectrometry. Mass change and ion intensity traces are shown below for each salt individually.

$Co(OAc)_2$ undergoes a straight forward reduction around 250°C producing a corresponding signal for ions of mass 44 u (CO_2) and forming a residue 36% of the initial mass consistent with almost total reduction to cobalt metal. This data suggests the salt rapidly decomposes into gaseous by-products and the reduced metal.
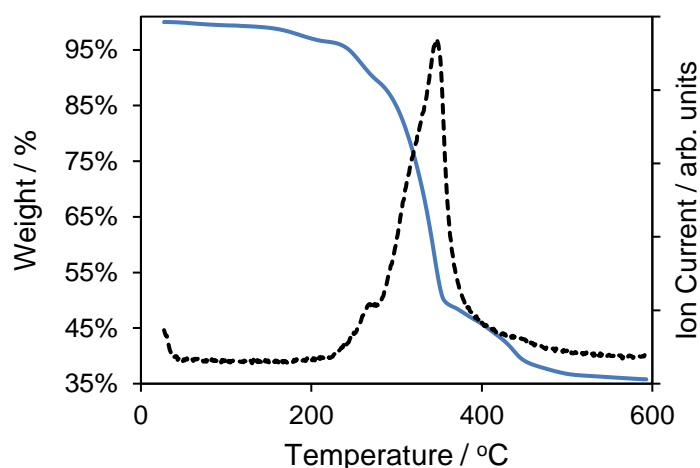
Figure S 4: Mass change (blue solid line) of $Co(OAc)_2$ under a reducing atmosphere. Mass traces of 44 u (dashed) produced by decomposition of the salt in the same temperature range.

The reduction of $CoCl_2·2H_2O$ begins with the loss of water in two steps (20% mass) followed by a prolonged stable phase before the reduction of the salt rapidly in the temperature range 450 °C – 600 °C (39%). During this rapid mass loss a significant spike is observed for ions of mass 36 u ($H^{35}Cl$) and 38 u ($H^{37}Cl$) indicating that the salt reduces directly into elemental metal and HCl gas.
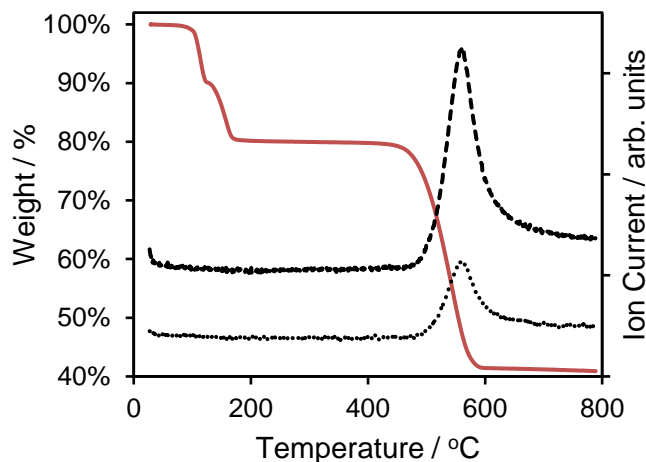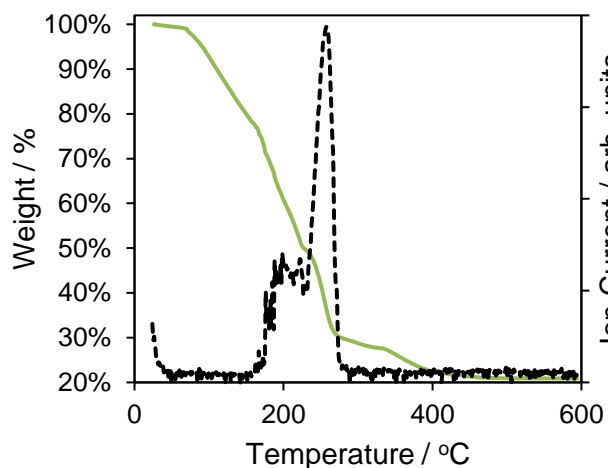

Figure S 5: Mass change (red solid line) of $CoCl_2$ under a reducing atmosphere. Mass traces of 36 u (large dash) and 38 u (small dash) produced by decomposition of the salt in the same temperature range.

The reduction of $Co(NO_3)_2·6H_2O$ is a more complex process, initially the salt melts with the loss of water starting at 55 °C, seen as the first sharp decrease in weight, this is followed by the loss of the nitrogen at 165 °C-265 °C producing NO as shown by the mass trace of 30 u below. Following the loss of the nitrogen there is a further mass loss, possibly the final reduction of a cobalt oxide or hydroxide into the metallic cobalt metal (21% mass) formed at 400 °C.

Figure S 6: Mass change (green solid line) of $Co(NO_3)_2$ under a reducing atmosphere. Mass trace of 30 u (dashed) produced by decomposition of the salt in the same temperature range.

Powder XRD

The x-ray diffraction patterns collected from the carbonization process were analysed using GSAS-II to complete a Rietveld fitting procedure, confirming the cobalt metal content. CIF files for both hcp and ccp metal phases were taken from the ICSD, instrument parameters and atom positions were fixed whilst the unit cell parameters and thermal parameters were permitted to vary during the fitting.
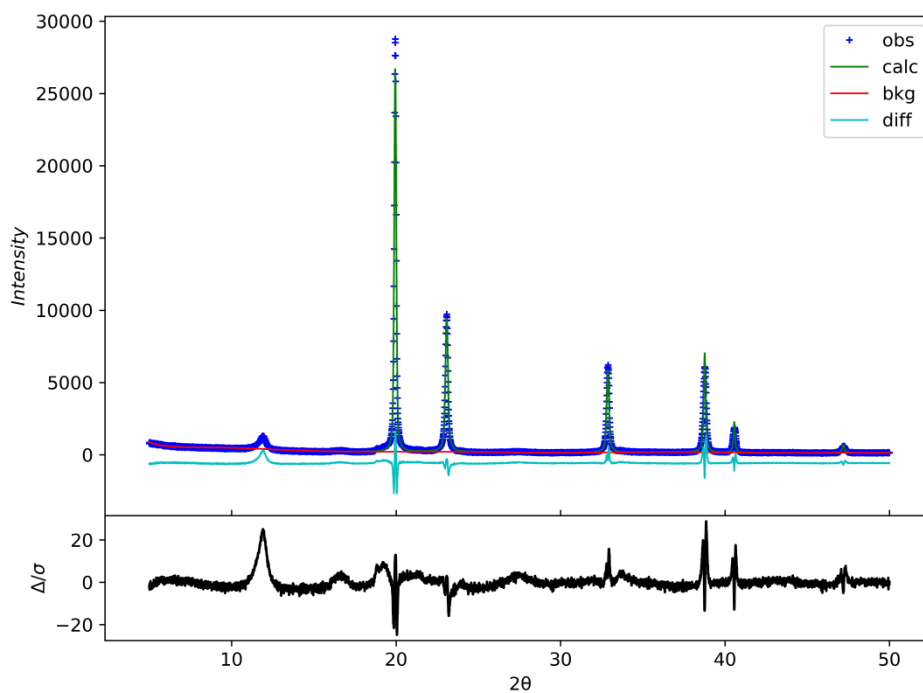

Figure S 7: Fitted powder XRD pattern of $Co(OAc)_2$ showing the calculated pattern of cubic cobalt metal.
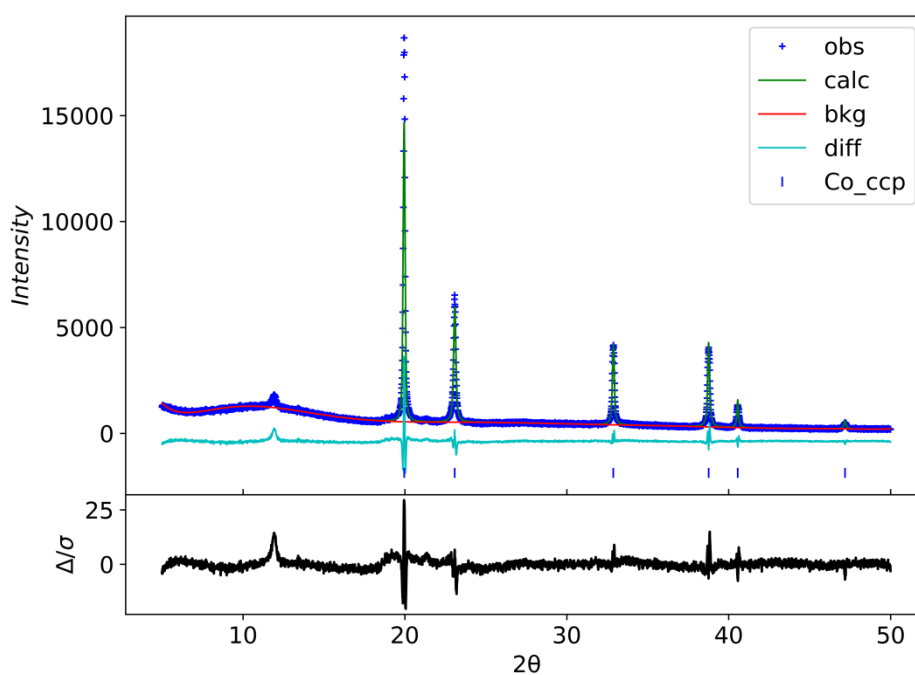
Figure S 8: Fitted powder XRD pattern of $Co(NO_3)_2$ showing the calculated pattern of cubic cobalt metal.
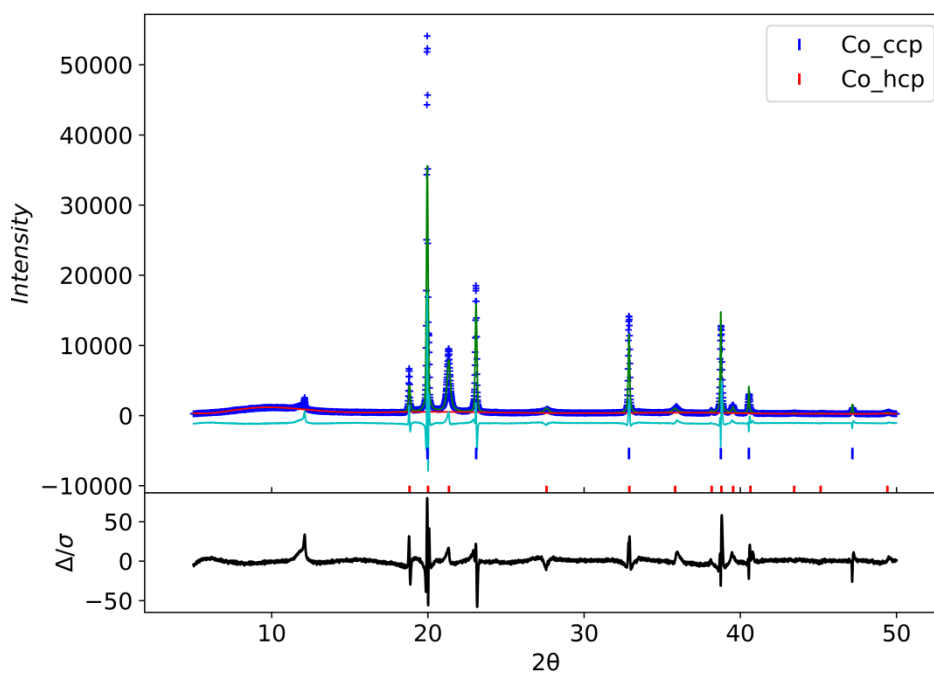
Figure S 9: Fitted powder XRD pattern of $CoCl_2$ showing the two phases of metal present and the calculated pattern.
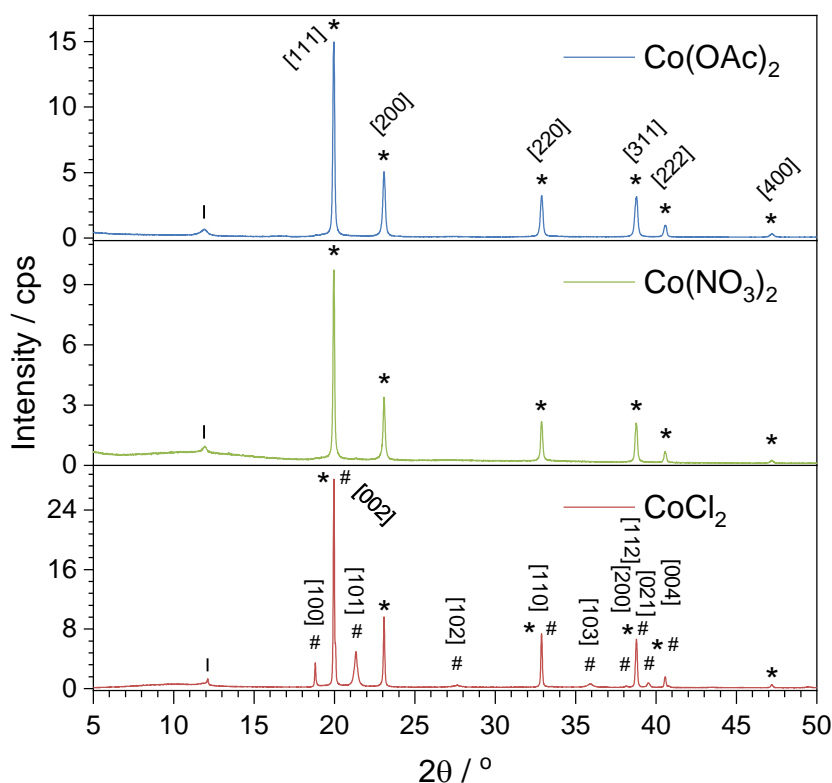
Figure S 10: Powder XRD patterns of carbonized foams containing Co metal produced in-situ; $Co(OAc)_2$ and $Co(NO_3)_2$ salts produced metal with exclusively ccp reflections (*) indexed in the top pattern. The $CoCl_2$ salt produced both hcp (#) and ccp (*) phases with only hcp peaks indexed.

After acid washing to remove all metal, the foams were re-analysed by capillary XRD. The patterns shown below do not contain any peaks attributed to metals; thus, the acid washing is effective at removing all crystalline metal particles. The diffractometer setup was the same in every case so differences in intensity are due to different sample densities, which affects the mass that can be packed into a capillary.
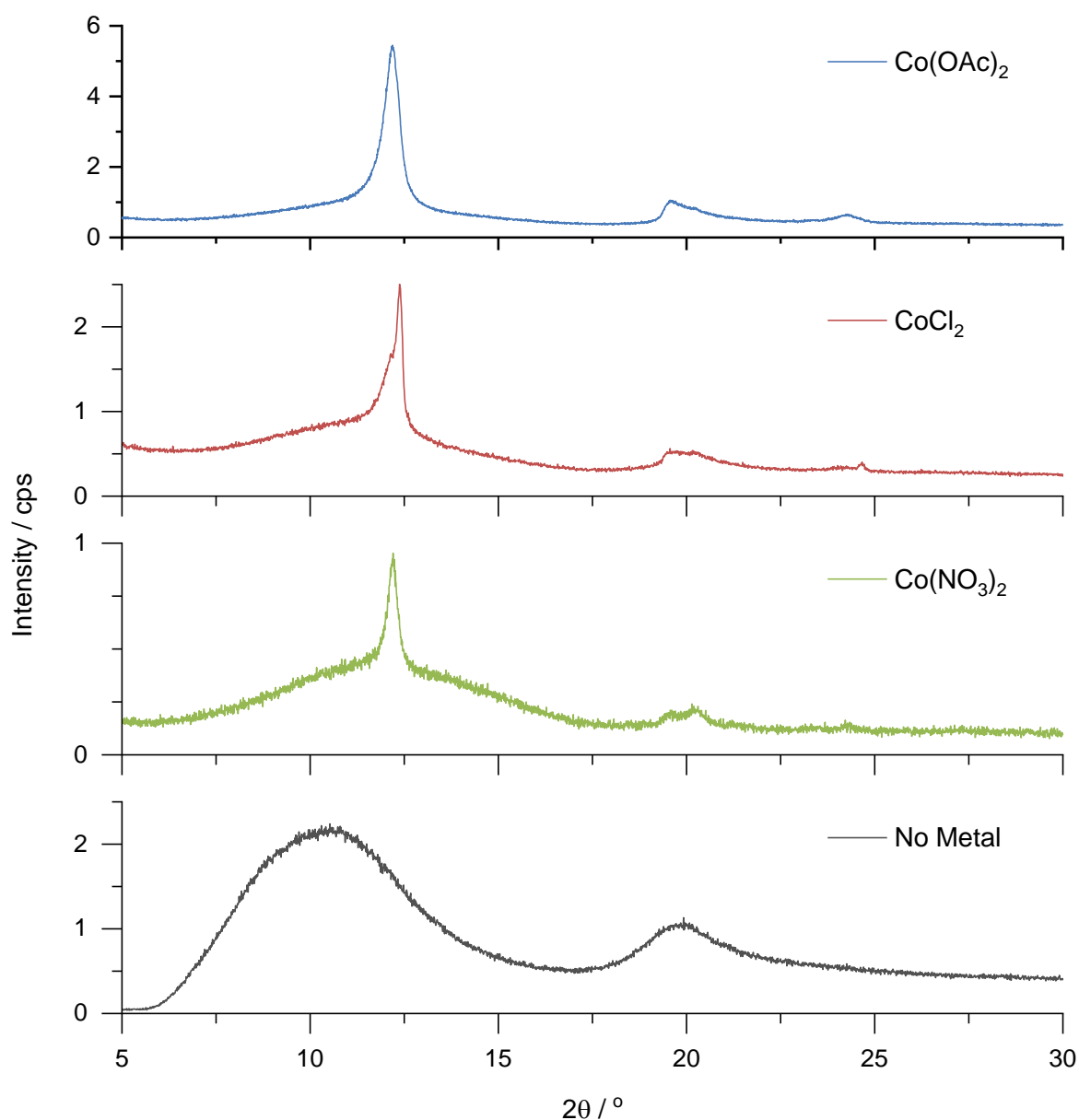
Figure S 11: Powder XRD patterns of carbon foams after acid washing (except metal free control), sample held in a capillary and recorded using an Mo source.

Raman Spectroscopy

Peak Fitting was done in Python3.7 using the freely available *lmfit* package for linear least squares regression.[1] The peak model used was a 6th order polynomial background with Lorentzian peak shapes used for the Raman spectral features. An algorithm was used to check the validity of each peak added to the model before returning data; in brief the reduced chi-squared metric was compared before and after every peak (G, D, 2D, D+G) was added to the model and any peak accounting for less than 2.5% improvement in goodness of fit was deemed to be due to the fitting of random noise rather than a meaningful peak, and thus reported with an intensity equal to zero. 3D bivariate histograms were then prepared with *MatPlotLib* to show the I_D/I_G and I_{2D}/I_G ratios simultaneously, with more populated bins denoted with a colour map.[2]

[1] M. Newville, T. Stensitzki, D. B. Allen and A. Ingargiola, , DOI:10.5281/ZENODO.11813

[2] J. D. Hunter, Comput. Sci. \& Eng., 2007, 9, 90–95.

Raman data was collected over a wide area by movement of an automated stage underneath a fixed microscope assembly that produced a laser focused onto the sample surface. The details of the area covered and the step size, or distance between points, is detailed below. Different samples had different map sizes and steps due to differences in surface smoothness.

Table S 2: Details of the area and spot distribution used for automated Raman analysis. An automated stage was moved under the lens with spectra recorded at every point.

Sample	x Distance / μm	x Step Size / μm	y Distance / μm	y Step Size / μm	Number of Points
CoAc$_2$	85	2.5	85	2.5	1156
CoCl$_2$	68	2.0	68	2.0	1156
Co(NO$_3$)$_2$	68	2.0	68	2.0	1156
Control	104	2.8	90	2.8	1184

Representative Raman spectra are shown below for each sample. These are generated from single data points that lie close to the average parameters from overall map fitting, in other words each is an individual spectrum that shows data representative of the centre of the distribution. The CoCl$_2$ spectrum is representative of the most common defective carbon but does not reflect the small quantity of graphite present.
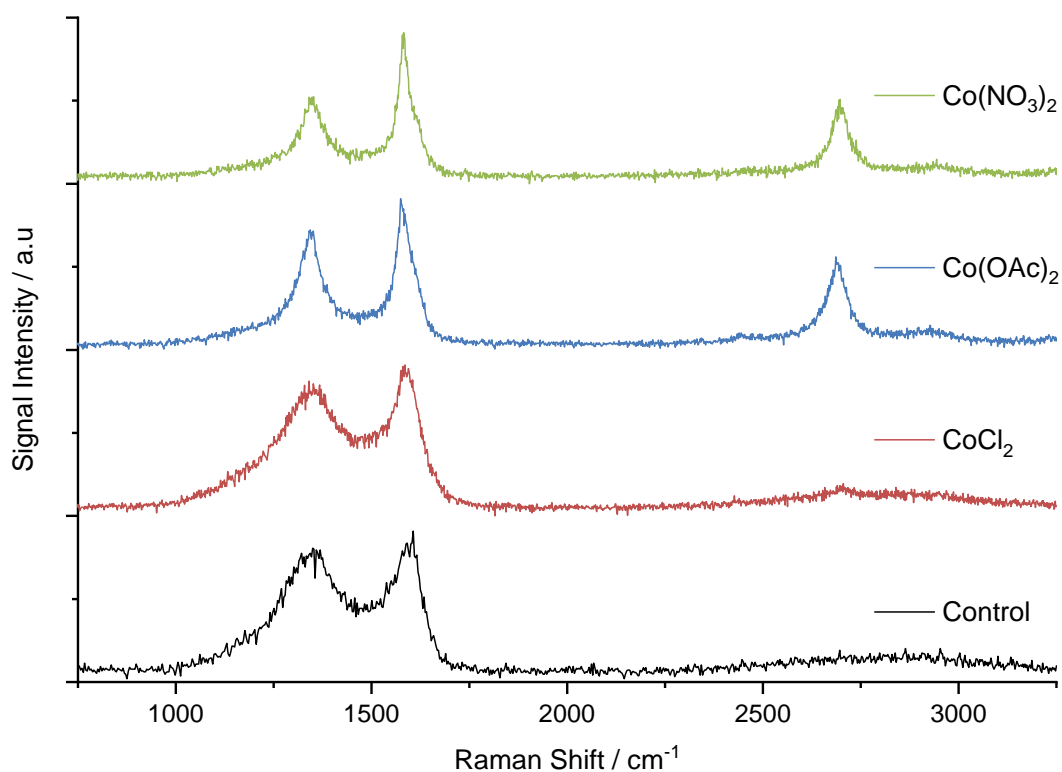
Figure S 12: Representative individual Raman spectra for each material. Intensity values are offset for clarity and normalized to allow visual comparison.

Pristine graphite (325 Mesh Flake Graphite supplied by Sigma Aldrich) was analysed for reference.
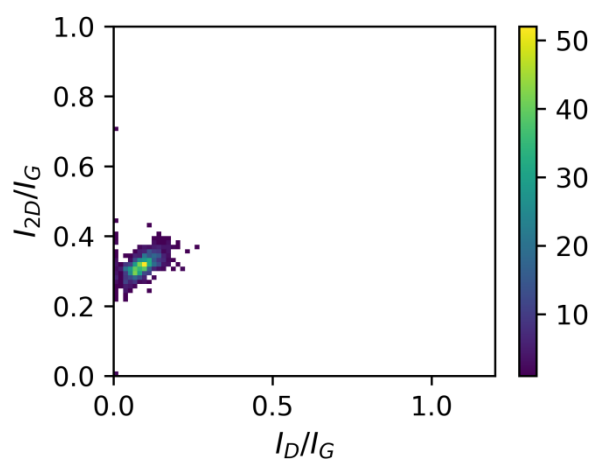
Figure S 13: Reference 3D bivariate histogram of pristine graphite; axis scale consistent with main plot (Figure 1).

Electron Microscopy

Additional images and analysis from electron microscopy data set.

SEM images of the $Co(NO_3)_2$ and $Co(OAc)_2$ based foams show a difference in morphology, with the nitrate based foam containing many thin flakes and holes with vary narrow wisps of carbon based material extending from the surface. In comparison the acetate based foam, whilst porous has a more solid, smooth surface at this magnification level and does not present any very thin edges extending from the bulk.
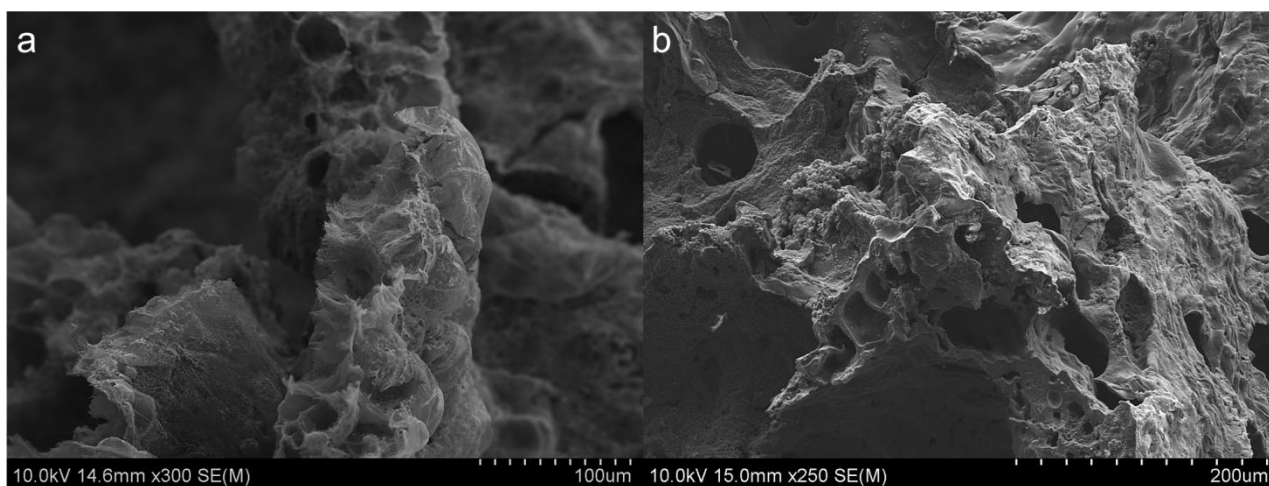
Figure S 14: Low magnification SEM images of (a) $Co(NO_3)_2$ based foam and (b) $Co(OAc)_2$ based foam showing the difference in morphology.

4.0kV 14.9mm x1.20k SE(L)   40.0um
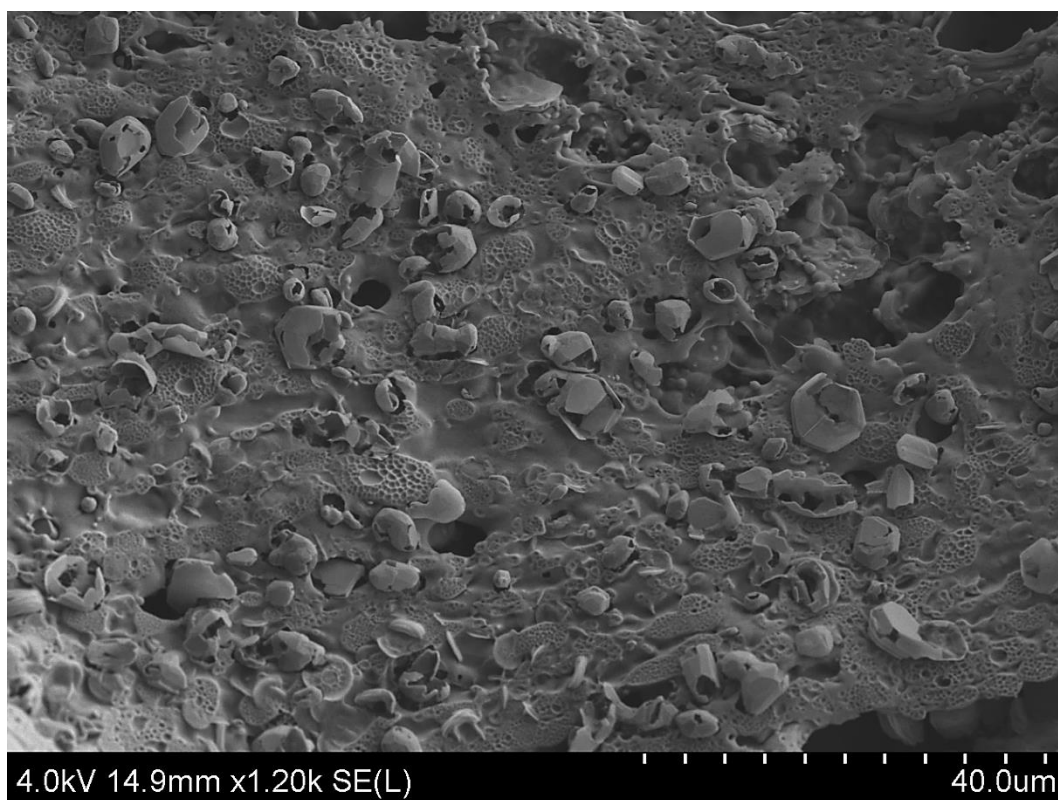
Figure S 15: Wide area SEM image of $CoCl_2$ after acid washing. The surface is covered with hollow carbon shells from graphite growth on crystalline metal particles that have been removed by acid washing.

10.0kV 14.6mm x2.50k SE(M)   20.0um
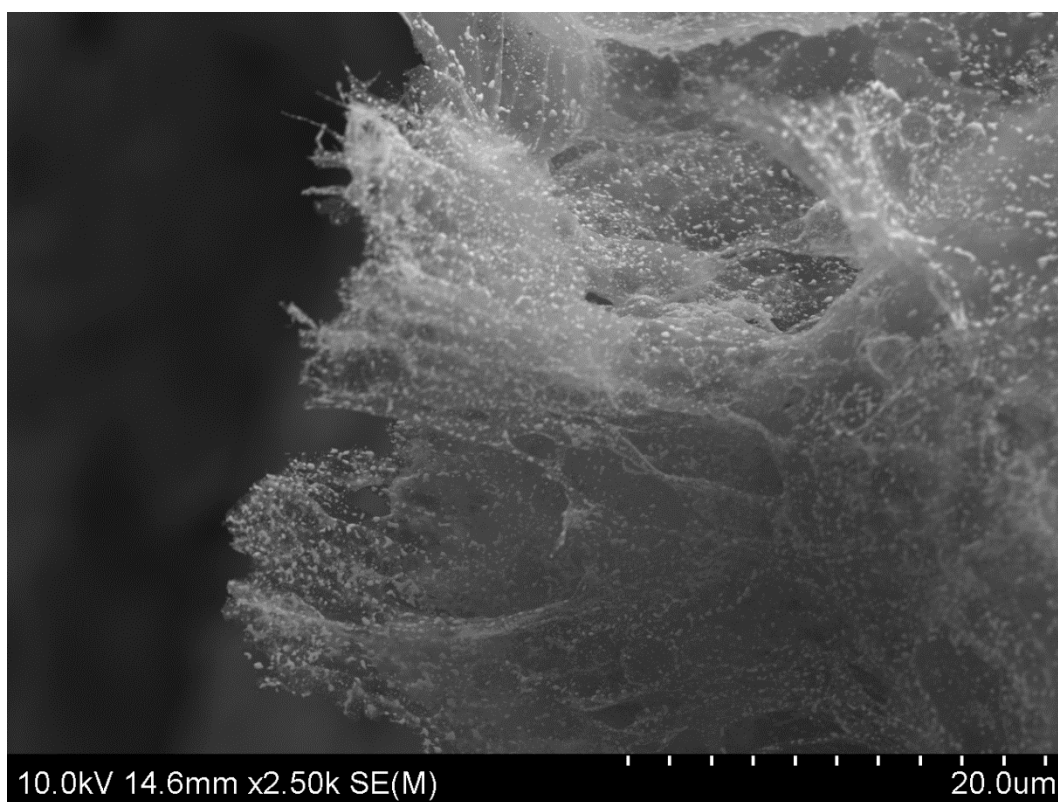
Figure S 16: SEM image of $Co(NO_3)_2$ before acid washing, taken at the edge of a foam. The carbon is made of thin fibrous material and brighter dots of metal particles, many larger than the nanoparticles observed in TEM are visible throughout.

Large area TEM images were used containing a large number of distinct circular particles. These were analysed with ImageJ by first converting them into binary black and white images highlighting only the nanoparticles by their contrast. Using the pixels these shapes were converted into particles sizes and the summary statistics are shown below. The nanoparticles produced from reduction of the acetate are much smaller than the particles from the nitrate; and the average size of the nitrate nanoparticles are a close match to the size of the holes observed in the structure after acid washing. The images used are included below.

Table S 3: Particle size summary statistics as measured by image analysis of transmission electron micrographs.

Image	P90 / nm	P50 / nm	P10 / nm	Mean / nm	SD / nm
Co(AC)2+M_0005	1.5	2.1	3.2	2.2	0.7
Co(AC)2+M_0001	1.5	2.0	2.9	2.1	0.6
Co(OAc)$_2$	**1.5**	**2.0**	**3.0**	**2.2**	**0.6**
29-1 Co(NO3)2+M_0006	9	10	17	11	3
29-1 Co(NO3)2+M_0005	9	10	16	11	3
Co(NO3)2+M_0005	6	9	14	9	3
Co(NO$_3$)$_2$	**7**	**10**	**15**	**10**	**3**
Co(NO$_3$)$_2$ Holes	**8**	**11**	**18**	**12**	**4**
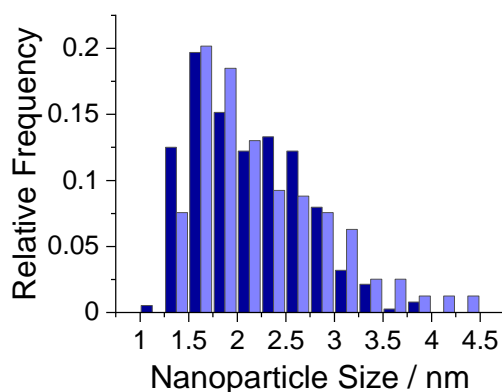
Figure S 17: Histogram of the particle size distribution as measured by transmission electron microscopy showing the particle size measured from the sample derived from Co(OAc)$_2$. The darker colour represents data extracted from the image labelled 0001 and the lighter colour the data from the image labelled 0005.
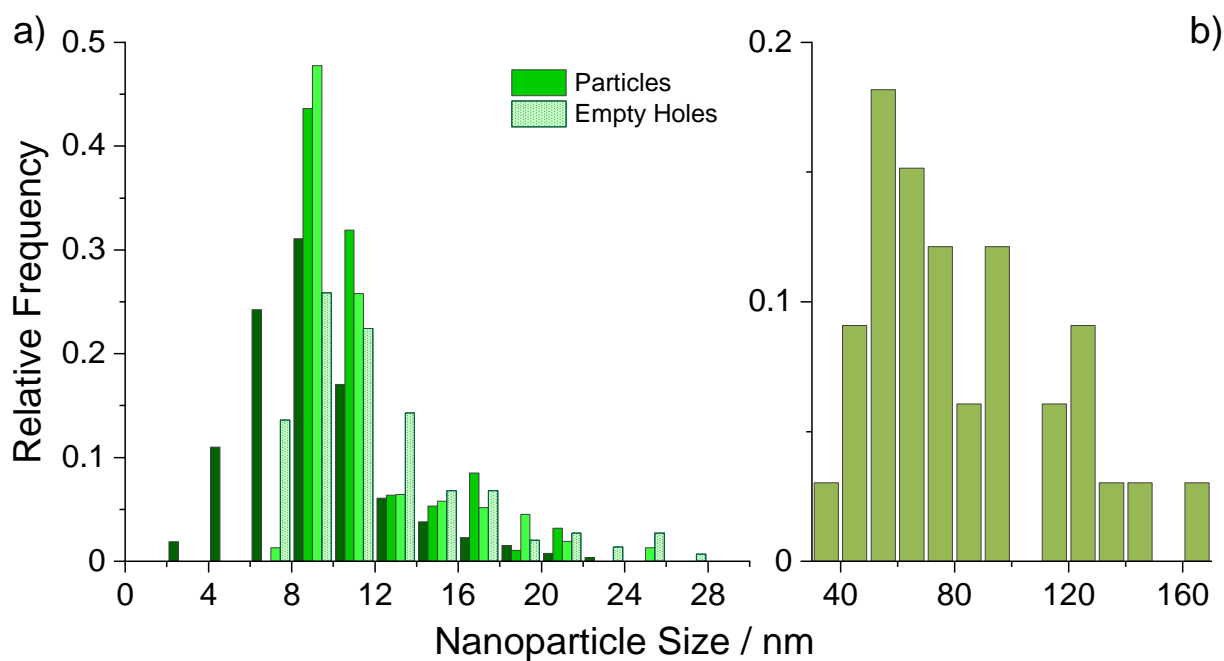
Figure S 18: Histograms of the particle size distribution as measured by transmission electron microscopy from the sample derived from Co(NO$_3$)$_2$. a) Smaller nanoparticles; the darkest colour, left most bar, represents data taken from the 0005 image, lighter bars are then 29-1 0005 and 29-1 0006 data respectively; the lightest bar on the right shows the size distribution of the empty voids left after washing. b) Larger nanoparticles crudely measured from the Co(NO$_3$)$_2$+M_0004 image.
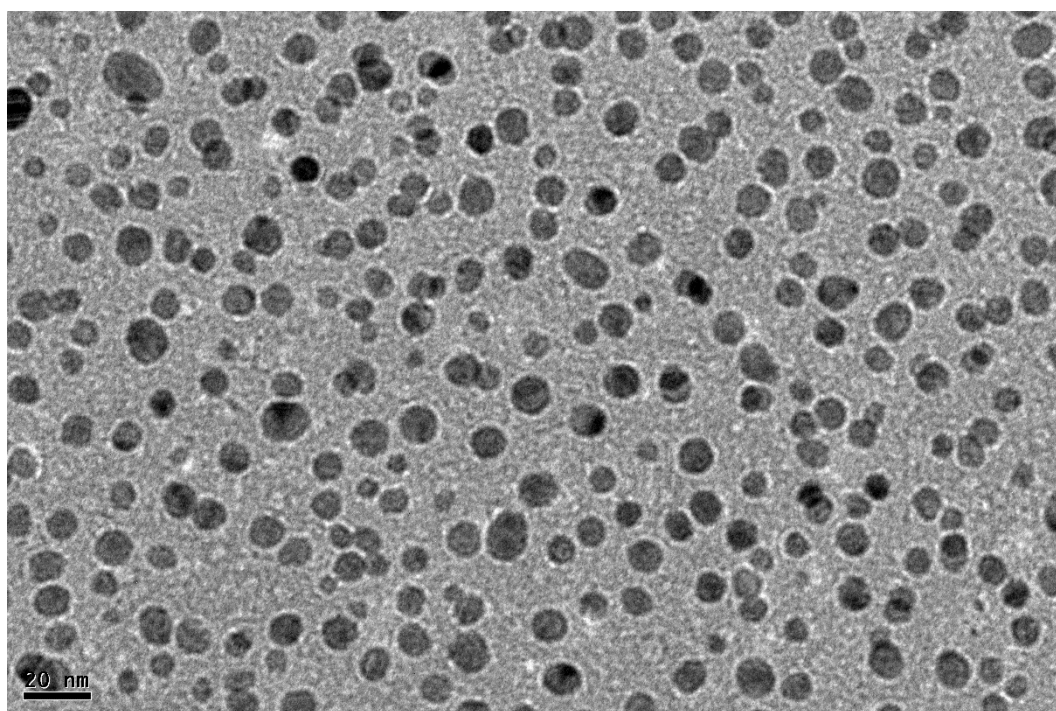
Figure S 19: TEM image of Co(NO$_3$)$_2$ derived sample used for particle size analysis. (Image label: *Co(NO3)2+M_0005*)
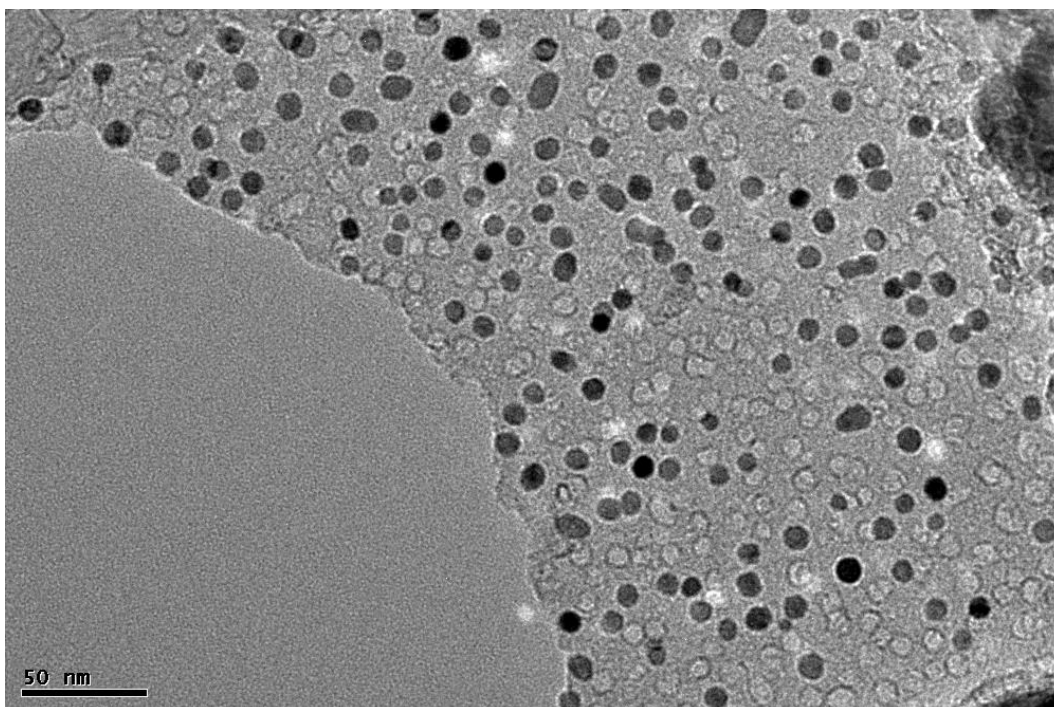
Figure S 20: TEM image of Co(NO$_3$)$_2$ derived sample used for particle size analysis. (Image label: *29-1 Co(NO3)2+M_0005*)
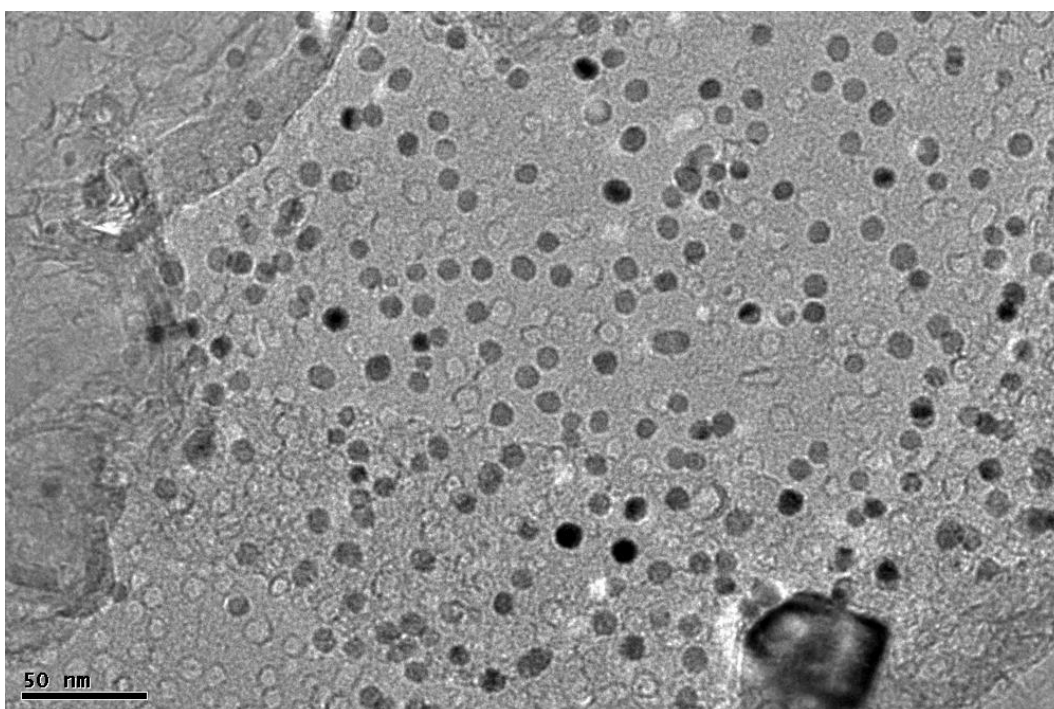
Figure S 21: TEM image of Co(NO$_3$)$_2$ derived sample used for particle size analysis. (Image label: *29-1 Co(NO3)2+M_0006*)
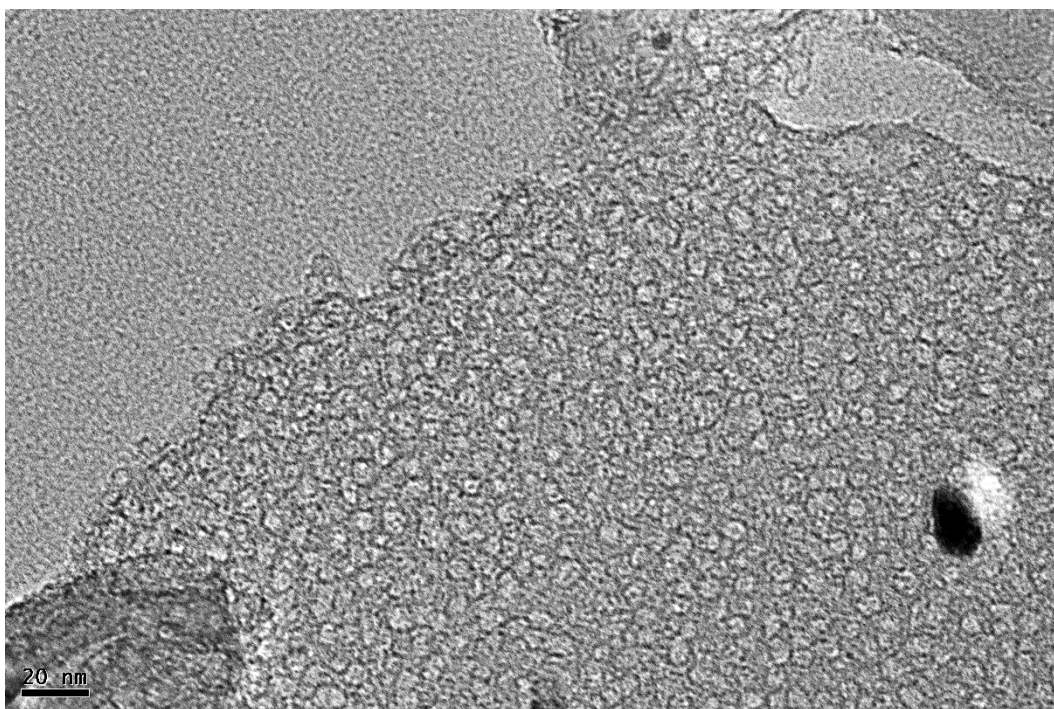
Figure S 22: TEM image of $Co(NO_3)_2$ derived sample used for size analysis of the holes left in the structure, seen as faint pale circles. (Image label: *Co(NO3)2+M_0007 holes*)
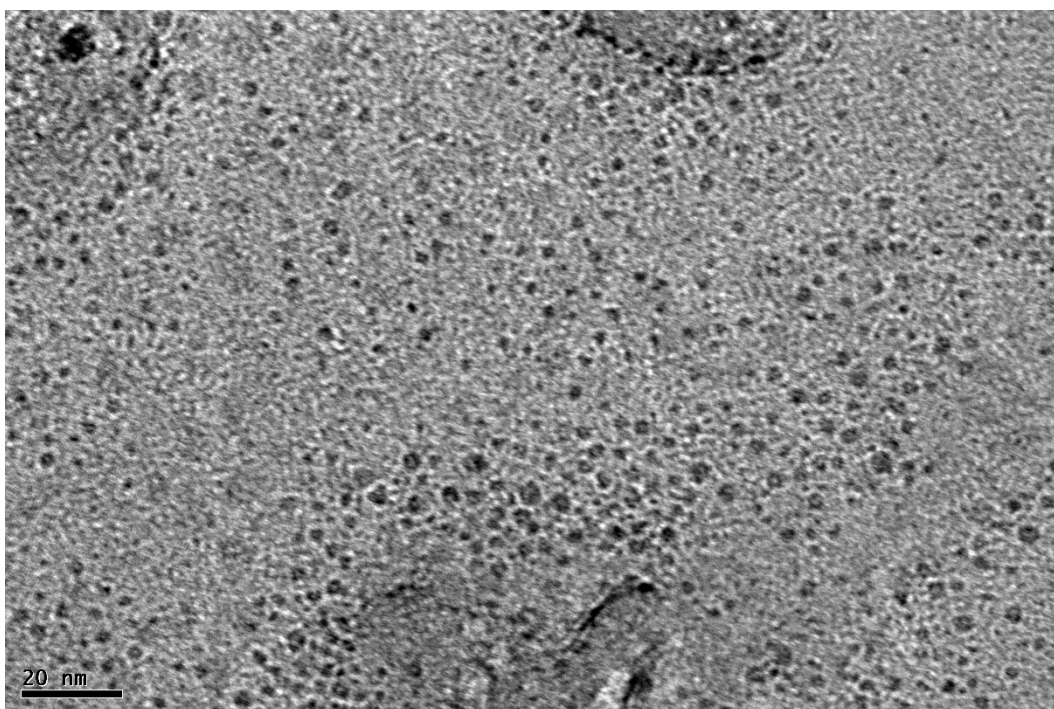
Figure S 23: TEM image of $Co(OAc)_2$ derived sample used for particle size analysis. (Image label: *Co(AC)2+M_0005*)
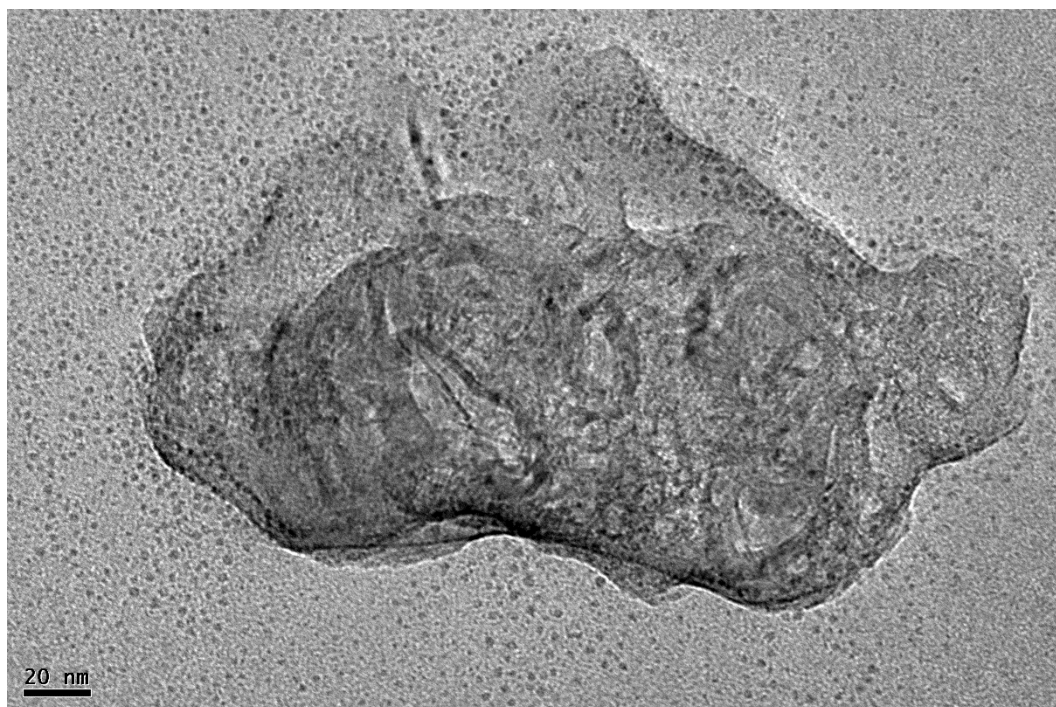
Figure S 24: TEM image of Co(OAc)$_2$ derived sample used for particle size analysis. (Image label: *Co(AC)2+M_0001*)
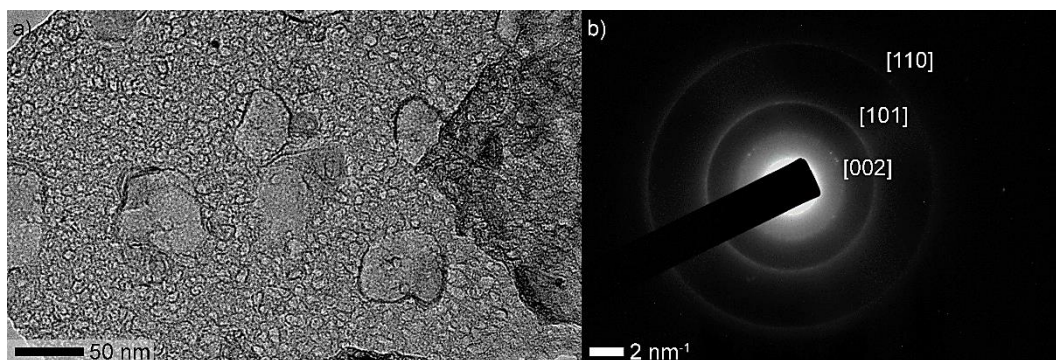
Figure S 25: a) Electron micrograph of graphene growth around metal nanoparticles removed by acid wash from Co(NO$_3$)$_2$ sample and b) the SAED pattern in the region shown with three rings visible and indexed to graphite.

TEM images of the carbonized foam from CoCl$_2$ derived metal catalyst; images shown for completeness however the bulk analysis shows the majority of material is amorphous carbon, whereas the sample preparation required for TEM analysis favours thin, flake like material by virtue of removing large aggregates.
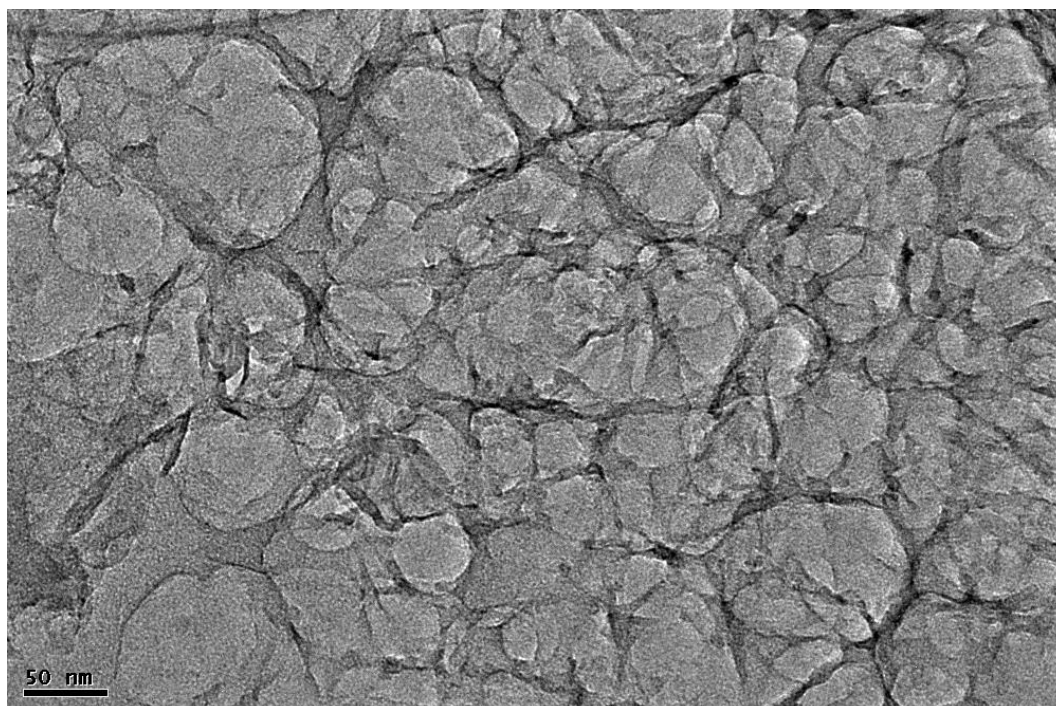
Figure S 26: TEM image of CoCl$_2$ derived sample showing fibrous network of amorphous carbon.
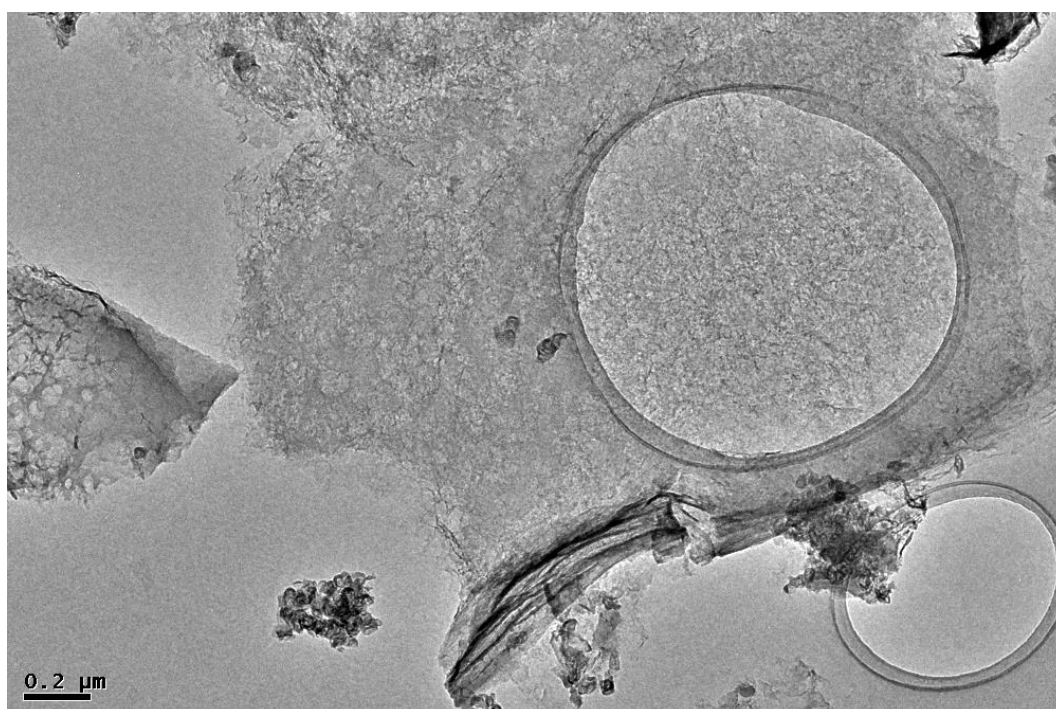
Figure S 27: Wider angle image of TEM showing a large flake of amorphous carbon with a thicker region of carbon upturned visible at the bottom. Possible minor fraction of carbon ribbons visible in the bottom left of the image.
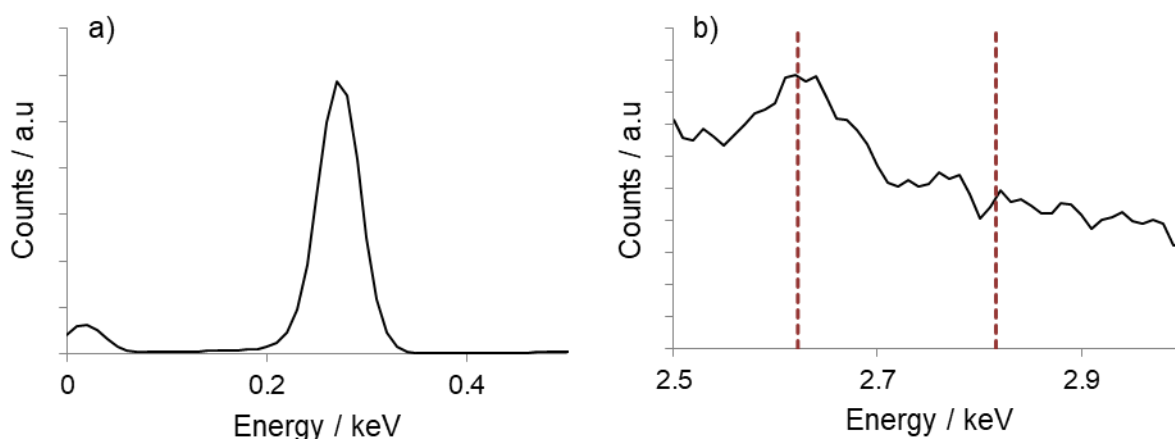
Figure S 28: EDX spectra from the CoCl$_2$ derived sample. a) x-ray counts from carbon K$_{\alpha1}$ emission; b) x-rays counts in the region expected from Cl K$_{\alpha1,2}$ with the expected energies shown by the dashed lines.

The carbonized foams extracted from the furnace work tube were washed in 6M HCl then filtered. The acid washings were analysed by ICP for cobalt content. The table below summaries the theoretical cobalt content, calculated from the total mass of cobalt added to the gel before carbonization divided by the total mass of material extracted from the carbonization before any washing. The foam was weighed before and after acid washing to determine the mass change during this process and the ICP was used to determine the cobalt washed out with acid. The difference between the theoretical cobalt content and mass lost during washing shows that whilst all of the expected metal from the Co(OAc)$_2$ and CoCl$_2$ was removed, there was less removed from the Co(NO$_3$)$_2$ sample than expected, supporting conclusions that some metal particles remained trapped within the structure. Furthermore, there was a more substantial mass changed from acid washing not accounted for by the metal content of the ICP analysis. One hypothesis is that the NO$_x$ gasses that etched the structure also produced some oxidised functional groups inside the porous structure that reacted and was removed in solution by acid washing; although this is speculation.

This data does however clearly illustrate the substantially greater fraction of carbon lost from the Co(NO$_3$)$_2$ sample during graphitization; the starting carbon to metal ratio was roughly consistent across samples and yet here the metal is a much greater fraction of the mass extracted for the Co(NO$_3$)$_2$ derived sample.

Table S 4: Mass changes during the acid washing steps for each sample; shown as weight percentages of the carbonized foam.

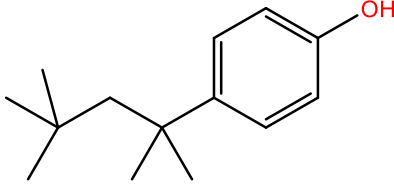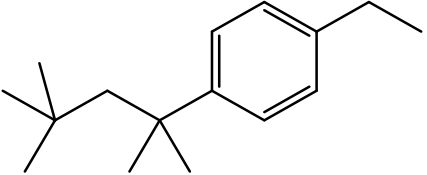| Sample	Theoretical Cobalt Content / wt.%	Total loss during acid wash / wt.%	Cobalt washed with acid / wt.%
Co(OAc)$_2$	58	59.39(2)	55.1(5)
CoCl$_2$	56	55.31(4)	53.0(6)
Co(NO$_3$)$_2$	79	71.02(4)	65.8(7)
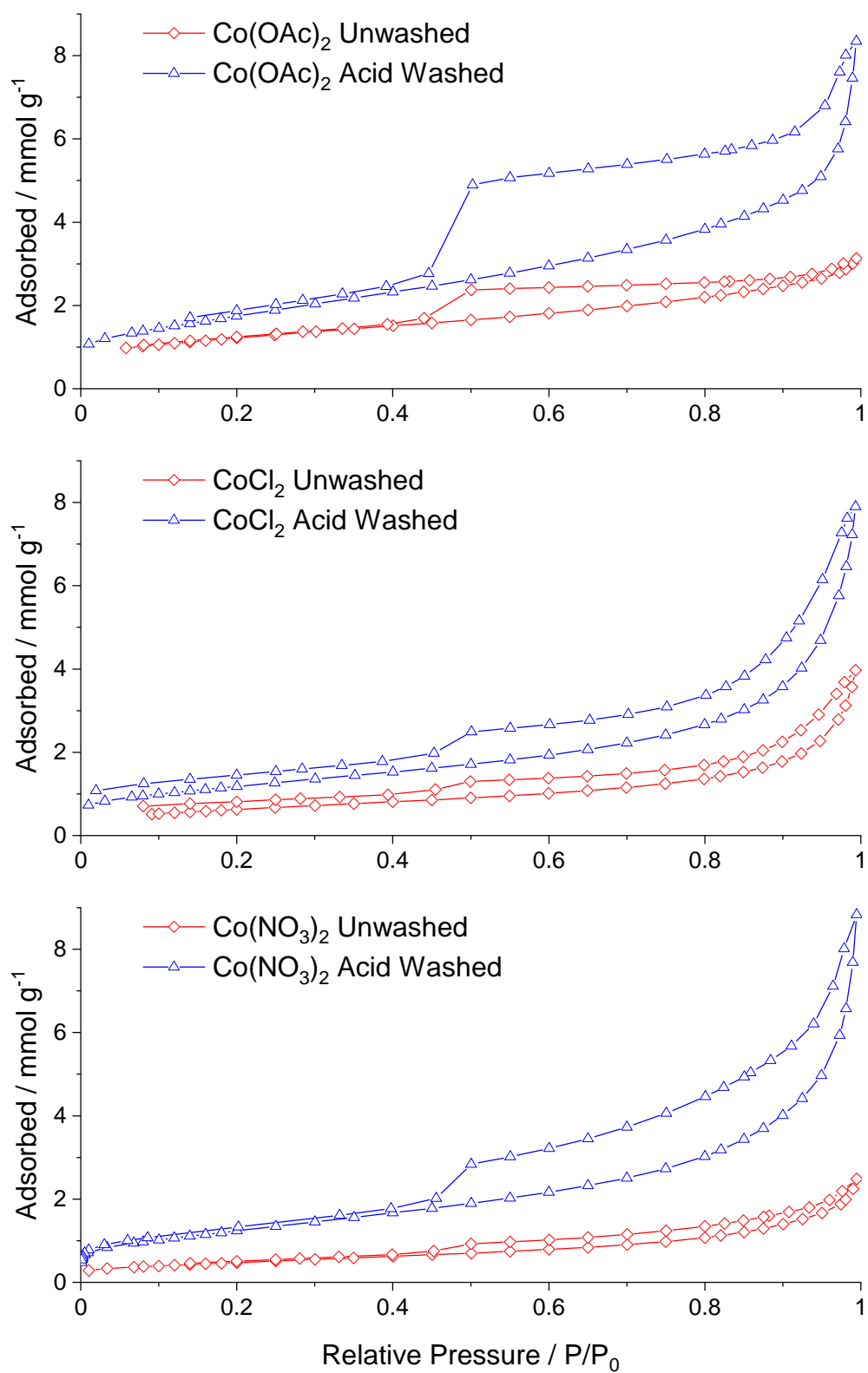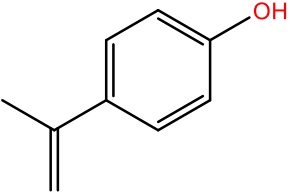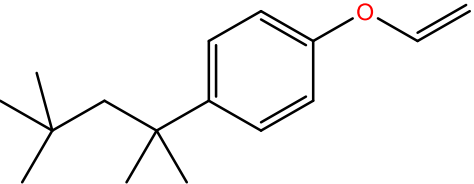
Figure S 29: N$_2$ sorption isotherms of porous samples before (red – bottom line) and after (blue – top line) washing with acid.

TritonX™-45 Control
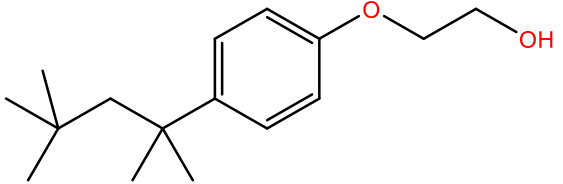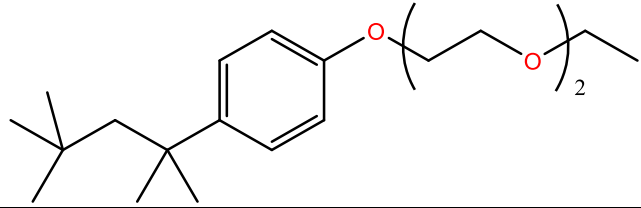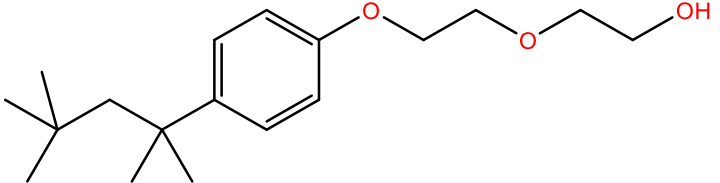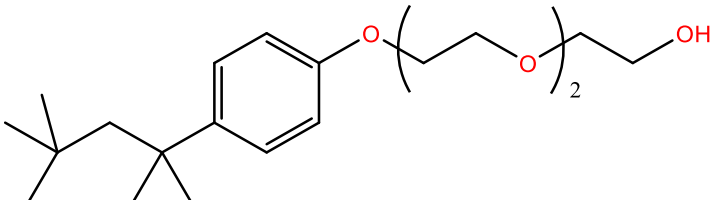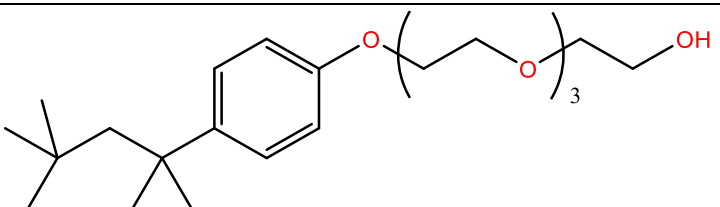
To ensure there is no significant difference with different quantities of Triton present relative to the hydrogen gas flow a number of samples were prepared. All peaks with intensity greater than 0.5% were assigned.
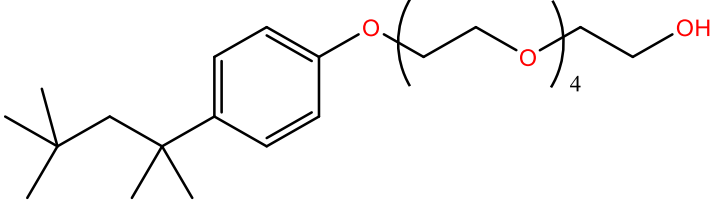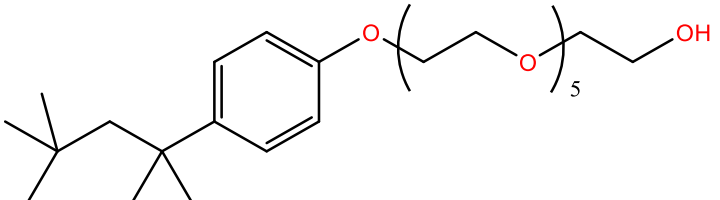
Table S 5: Summary of gas chromatography peaks and assignment based on mass spectrometry data.

Retention Time / min	% Intensity per mass of TritonX™			Molecular m/z	Structure
	0.8617g	1.3563g	1.6651g		
3.930(0)	-	0.5	0.5	**134**	
4.323(0)	-	0.7	0.8	**232**	
4.593(0)	0.7	1.6	2.1	**206**	
4.663(0)	0.6	0.7	0.8	**218**	
4.973(0)	5.4	3.3	3.9		*Peak present in solvent blank*

5.213(0)	2.3	2.4	2.6	**250**	
5.410(0)	2.6	1.6	1.9	*Peak present in solvent blank*				
5.793	-	-	0.5	**322**	
5.842(2)	14.5	13.8	14.5	**294**	
6.399(2)	25.5	22.1	23.4	**338**	
7.009(5)	24.2	25.5	24.8	**382**	
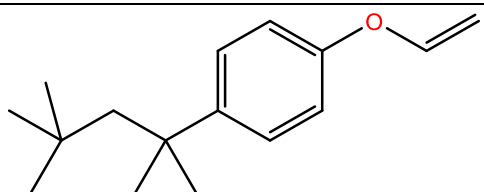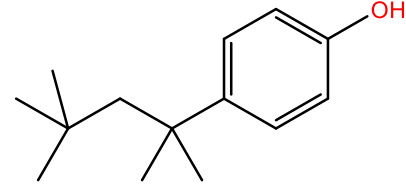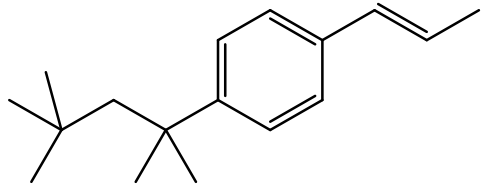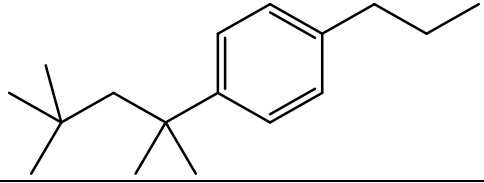
7.997(7)	15.4	18.6	16.6	**426**	
9.513	-	-	0.6	*Mass fragments consistent with TritonX^{TM} decomposition. However intensity too small for assignment.*	
9.78(1)	6.3	8.2	5.9	**470**	
Total	97.5 %	99.0 %	98.9 %		
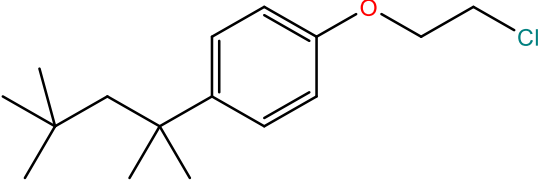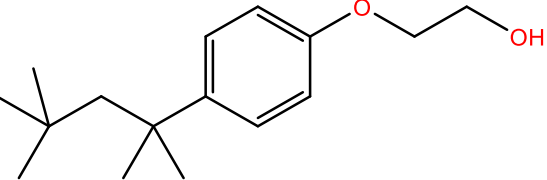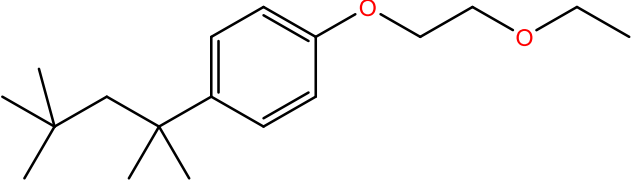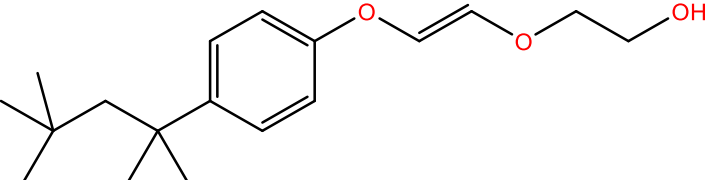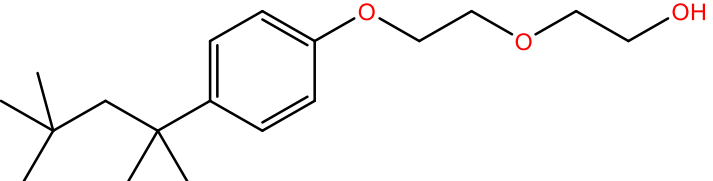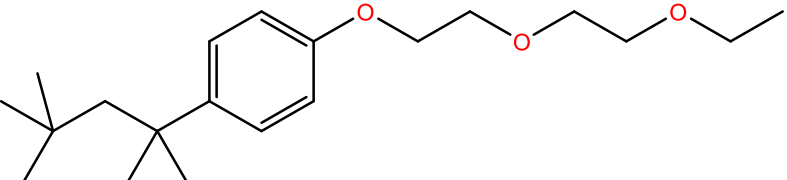
Cobalt Containing Gels

Peaks with intensity greater than 1% listed for comparison with proposed structures consistent with the mass spectrum shown. Not all peaks are observed for every sample.

The unsaturated compounds are shown with double bonds at the chain end however it is not possible to assign to double bond exactly.
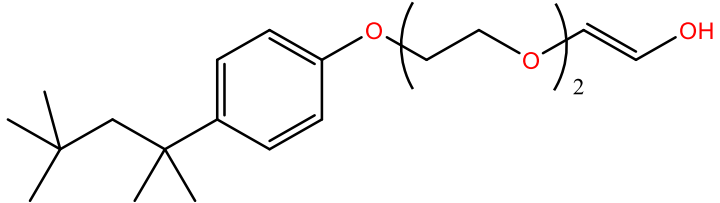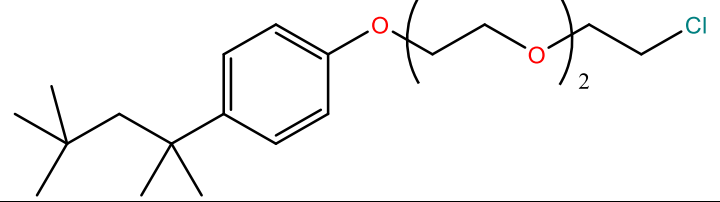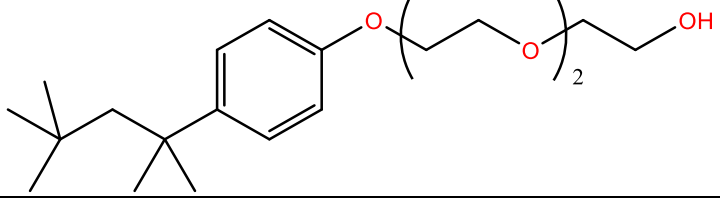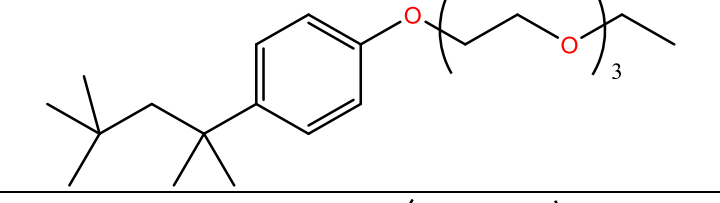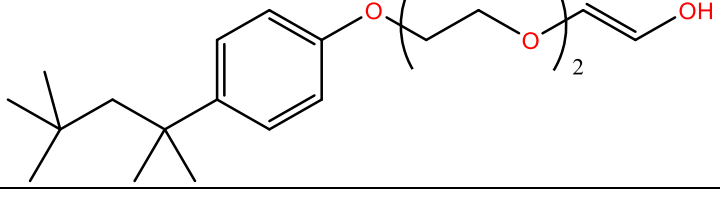
Table S 6: Summary of gas chromatography data and assignment based on mass spectrometry data for carbonized samples with cobalt salt present.

Retention Time / min	Precursor Used			Present in Control?	Molecular m/z	Possible Structure
	CoAc$_2$	CoCl$_2$	Co(NO$_3$)$_2$			
4.323	1.3%	-	-	✓	232	
4.593	3.9%	10.6%	11.9%	✓	206	
4.613	0.5%	1.1%	-	✗	230	
4.847	-	1.6%	-	✗	232	
4.883	-	-	1.7%	✗	251	?
4.973	4.0%	5.7%	13.5%	✗		*Peak present in solvent blank*
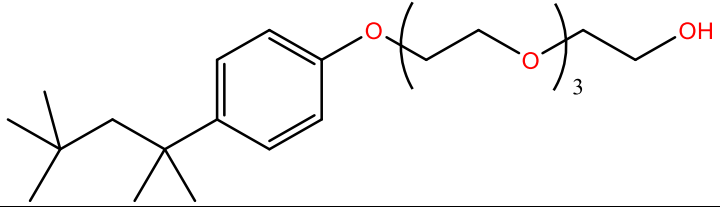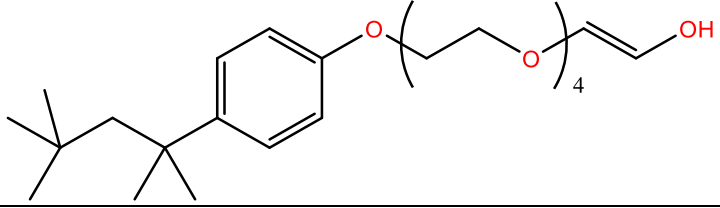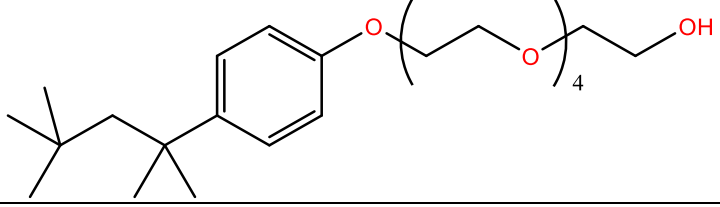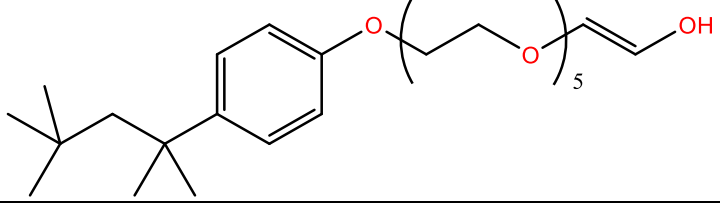
5.153	-	10.2%	-	✘	268	
5.213	2.7%	16.7%	14.4%	✔	250	
5.350	-	1.0%	1.9%	✘	278	
5.410	1.9%	2.8%	6.6%	✔	*Peak present in solvent blank*	
5.48	3.0%	1.2%	-	✘	292	
5.840	8.3%	18% OH (10% Cl)	15.1%	✔	294	
5.973	-	1.6%	2.5%	✘	322	

6.08	13.3%	1.2%	-	✘	336	
6.373	-	2.8%	-	✘	356	
6.399	10.9%	9.4%	15.2%	✔	338	
6.500	-	0.7%	2.2%	✘	366	
6.603	17.7%	-	-	✘	380	

6.995	7.1%	2.9%	6.7%	✓	382	
7.300	16.0%	-	-	✗	424	
7.997	2.2%	-	1.4%	✓	426	
8.490	8.3%	-	-	✗	468	
Total	99.8%	97.7%	94.4%			

Figure S 30: Gas chromatography trace of the oil extracted from the Co(OAc)$_2$ sample carbonization.
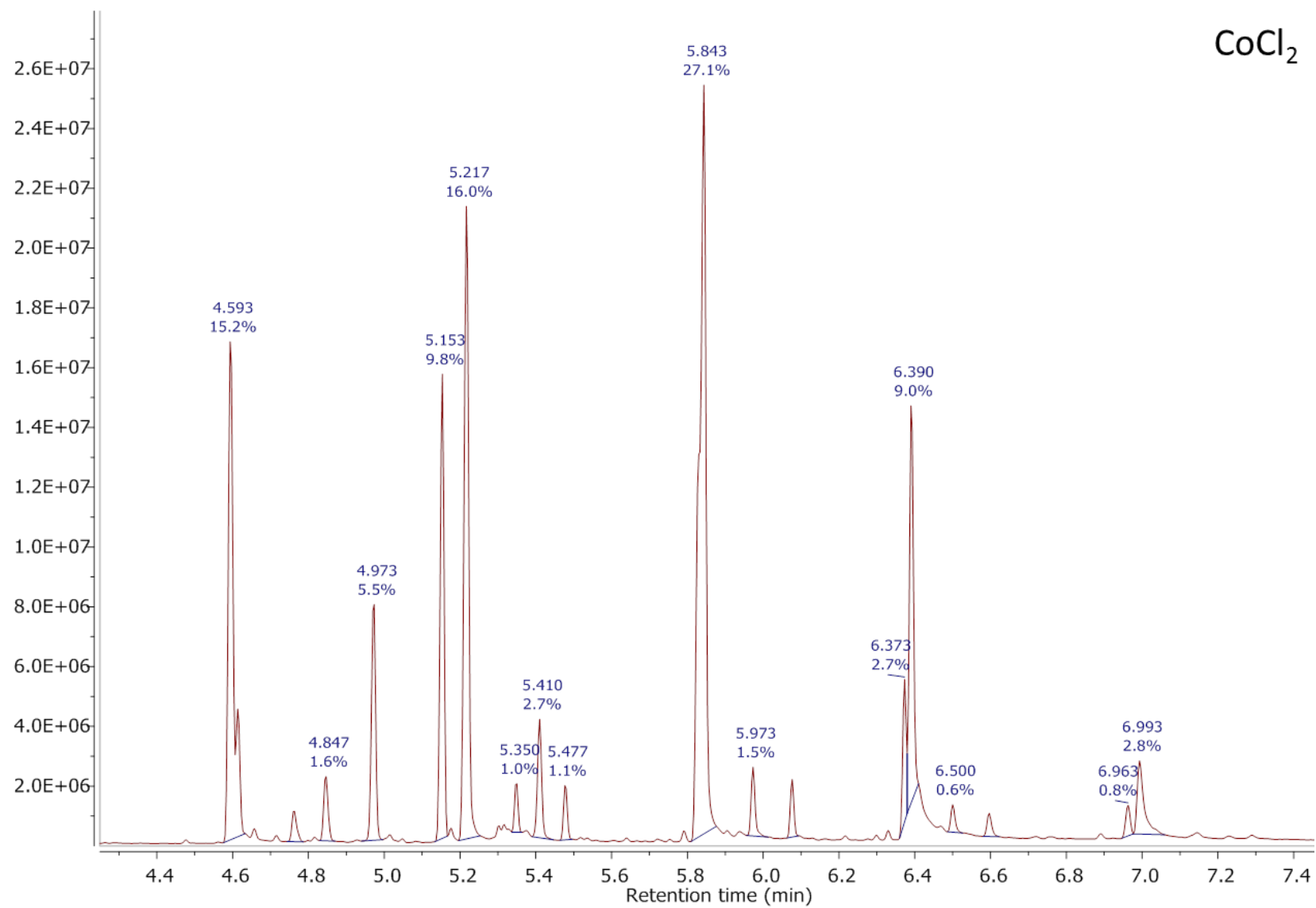
Figure S 31: Gas chromatography trace of the oil extracted from the CoCl2 sample carbonization.
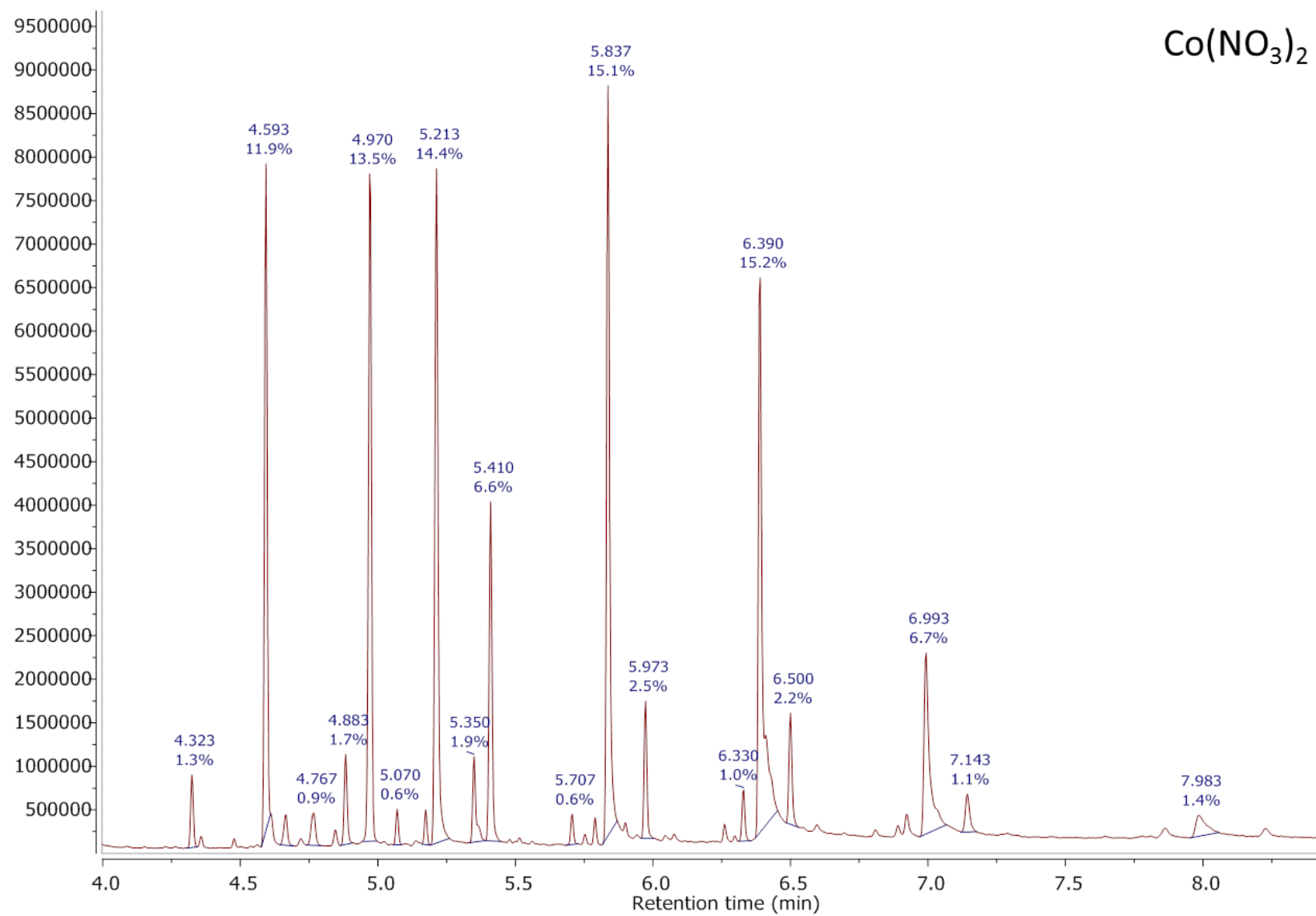
Figure S 32: Gas chromatography trace of the oil extracted from the Co(NO₃)₂ sample carbonization.
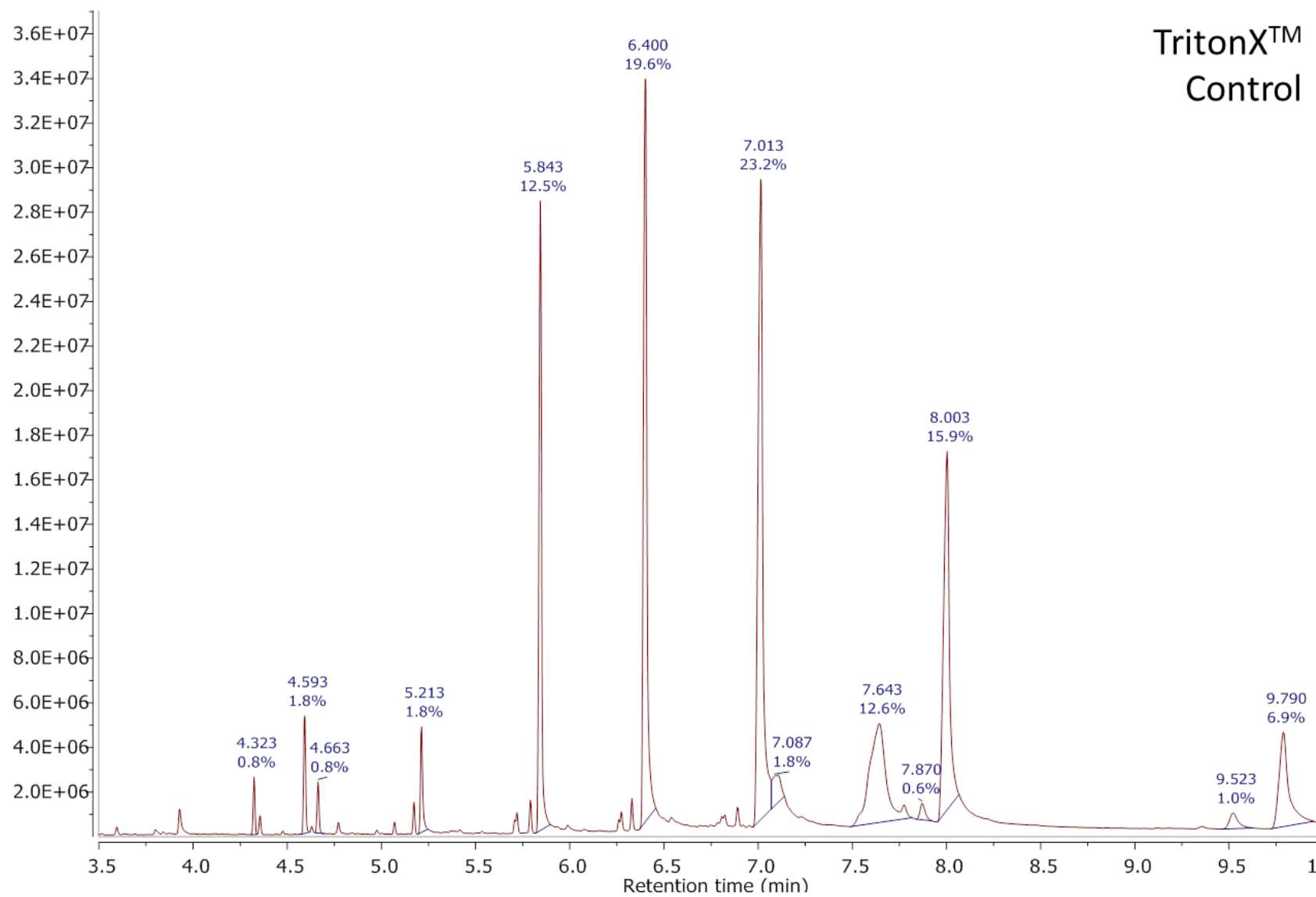
Figure S 33: Gas chromatography trace of the oil extracted from the metal free control carbonization.